ORIGINAL PAPER

Exploration of the structural, optoelectronic, magnetic, elastic, vibrational, and thermodynamic properties of molybdenum-based chalcogenides A_2MoSe_4 (A =Li, K) for photovoltaics and spintronics applications: a first-principle study

Muhammad Ali[1] · R.M. Arif Khalil[1] · Muhammad Iqbal Hussain[2] · Fayyaz Hussain[1]

Abstract

Context In the present work, the cubic phase of the chalcogenide materials, i.e., A_2MoSe_4 (A =Li, K) is examined to explore the structural, optoelectronic, magnetic, mechanical, vibrational, and thermodynamic properties. The lattice parameters for Li_2MoSe_4 are found to be a= 7.62 Å with lattice angles of $\alpha=\beta=\gamma=90°$ whereas for K_2MoSe_4, a= 8.43 Å, and $\alpha=\beta=\gamma=90°$. These materials are categorized as semiconductors because Li_2MoSe_4 and K_2MoSe_4 exhibit direct energy band gap worth 1.32 eV and 1.61 eV, respectively through HSE06 functional. The optical analysis has declared them efficient materials for optoelectronic applications because both materials are found to be effective absorbers of ultraviolet radiations. These materials are noticed to be brittle while possessing anisotropic behavior for various mechanical applications. The vibrational properties are explored to check the thermal stability of the materials. On the basis of thermodynamics and heat capacity response, Li_2MoSe_4 is more stable than K_2MoSe_4. The results of our study lay the groundwork for future research on the physical characteristics of ternary transition metal chalcogenides (TMC).

Methods These physical properties are explored for the first time while using a first-principles approach based on density functional theory (DFT) in the framework of Cambridge Serial Total Energy Package (CASTEP) by Perdew-Burke-Ernzerhof generalized gradient approximation (PBE-GGA) functional. However, GGA+U and HSE06 are also employed to improve electronic properties. Kramers–Kronig relations are used to evaluate the dielectric function with a smearing value of 0.5 eV. Voigt-Reuss-Hill approximation is used for seeking the elastic response of these materials. The thermodynamic response is sought by harmonic approximation. The density functional perturbation theory (DFPT) approach is used for investigating atomic vibrations.

Introduction

An ongoing thrust in the world of materials science is the quest for new semiconductor materials. It is crucial to foster the growth of integrated circuits and optoelectronics in contemporary technology. So TMC has sparked a lot of consideration in the realm of materials, physics, and chemistry research owing to their extraordinary physical and chemical characteristics, such as superconductivity [1, 2], thermoelectricity [3, 4], charge density wave [5], and electro-catalysis [6, 7]. Due to their fascinating structures and peculiar properties, precious metal chalcogenides are the main subject of our research [8–10].

These materials, which have the basic chemical formula ABX_n, where A is an alkali metal, can be produced through

✉ Muhammad Iqbal Hussain
miqbal@ue.edu.pk

R.M. Arif Khalil
muhammadarif@bzu.edu.pk

Fayyaz Hussain
fayyazhussain248@yahoo.com

[1] Materials Simulation Research Laboratory (MSRL), Department of Physics, Bahauddin Zakariya University, Multan 60800, Pakistan

[2] Department of Physics, University of Education, Lahore 54000, Pakistan

solid-state reactions or by intercalating an A^+ atom into an BX_n lattice [11]. Additionally, they are renowned ionic conductors, making them an appealing family of inorganic compounds [12, 13]. In terms of alkali metal transition selenides, we specifically point out the emergence of the mixed-valent layered metal $NaCu_6Se_4$ [14], the mixed-valent two-dimensional metal $NaCu_4Se_3$ [15], and the two-dimensional metal $NaCu_4Se_4$, which demonstrates high hole mobility and enormous magnetoresistance [16]. The researchers also investigated the entire family of materials by creating and characterizing $CsCu_5S_3$ and suggesting $CsCu_5Te_3$. Since then, $CsCu_5Se_3$ has been produced in a phase that has been suggested as a performance-driven thermoelectric [17], and an ab initio study has been conducted to investigate the defect physics of $CsCu_5Se_3$ and its potential applications in optoelectronics [18]. To emphasize the potential for new materials, $CsCu_5Se_3$ and other novel chalcogenides are contrasted to their oxide analogues in a recent review on chalcogenides for photovoltaic uses [19]. Recent developments worth highlighting encompass the emergence of novel transition metal chalcogenide perovskites. The interaction of alkali-metal (A+) and chalcogen (X = S, Se, Te) chemistry offers solar-cell absorbers with electronic properties comparable to hybrid perovskites [20–22]. TMCs have considerable advantages, including their high resistance to decomposition [23, 24] as well as their flexible composition, structural, electrical, and optical properties. The need for solar energy is on the rise globally, which gives researchers diverse possibilities to create versatile optoelectronic devices that can use visible electromagnetic radiation and turn it into electrical energy. The molybdenum-based new combinations of ternary chalcogenides that are being studied for this reason appear to be practical for optoelectronic applications due to their strong optical conductivity and absorptivity. The purpose of the present investigation is to model A_2MoSe_4 (A=Li and K), a compound chemically similar to the recognized sodium molybdate (Na_2MoO_4) [25], in the solid-state with the project database [26]. Mebarki et al. [27] also explored the similar materials.

We can find out more about the physics of Na_2MoSe_4 crystalline form and its relatives by simulating them. We use a crystal structure prediction technique combined with Kohn–Sham DFT to figure out the ground state properties of this alkali metal TMC. We were inspired to further investigate this domain in the area of ab initio studies by earlier research on TMC and other effective chalcogen-based materials. So, we chose another series of novel chalcogenides that combine alkali atoms with Mo atoms. According to the literature, no experimental or computational studies exist on A_2MoSe_4 (A =Li, K) the novel combination of molybdenum-based chalcogenide materials are documented to date. The chalcogenide phases have significance in batteries, solar cells, flexible electronics, fiber-optic energy storage, and catalysis applications, thus, we got inspired by this challenge to computationally inspect the structural, optoelectronic, magnetic, mechanical, vibrational, magnetic, and thermodynamic properties of A_2MoSe_4 (A =Li, K) for the first time while using CASTEP code.

Computational methodology

All calculations for A_2MoSe_4 (A=Li, K) are performed using a DFT-based CASTEP simulation code [28, 29]. The non-conserving pseudopotentials [30–32] are preferred to model electron-ion interactions. In addition, PBE-GGA [33], GGA+U with the Hubbard value of 6 eV for Mo element [34], and HSE06 [35] functionals are used to examine the electronic properties. In order to achieve refined structural properties, the plane wave cutoff energy of 400 eV is chosen to converge these systems. To obtain a converged and extremely precise electronic density of states, the instrumental smearing value of 0.5 eV is utilized. A kinetic energy cutoff of 350 eV is chosen for both chalcogenides and Monkhorst–Pack [36] k-point mesh 5×5×5 is chosen from the first Brillouin zone (BZ). The optical properties are investigated by solving the Kohn–Sham equation and Kramers–Kroning relations [29, 37–39]. Utilizing the Voigt–Reuss–Hill approximation [40, 41], the mechanical strength of A_2MoSe_4 (A=Li, K) is determined. DFPT [42] is employed to illustrate phonon frequencies in order to calculate thermal stability. Thermodynamic properties are determined by harmonic approximation [43].

Discussions on the results

Structural properties

To investigate the structural stability and optimization, the energy vs. volume graph for A_2MoSe_4 (A=Li, K) is construed using the PBE-GGA functional. As can be seen in Fig. 1, the crystal structures in the cubic phase with the space group (Fd-3m) and point group Oh(m-3m) are optimized. It is noticed that the A_2MoSe_4 (A=Li, K) unit cell comprises 14 atoms, including two molybdenum atoms, eight Se atoms, and four Li atoms. As shown in Fig. 2a, b, the energy vs. volume optimization graph for the A_2MoSe_4 (A=Li, K) compounds in the cubic phase is displayed in accordance with the Birch–Murnaghan relationship [44]. Table 1 lists the computed values of the lattice constant, ground state energy, and volume at static equilibrium and bulk modulus. As per the literature survey, neither experimental nor theoretical values of the lattice parameters, and bulk modulus are available to compare with our computed results. The studied compounds achieved their equilibrium
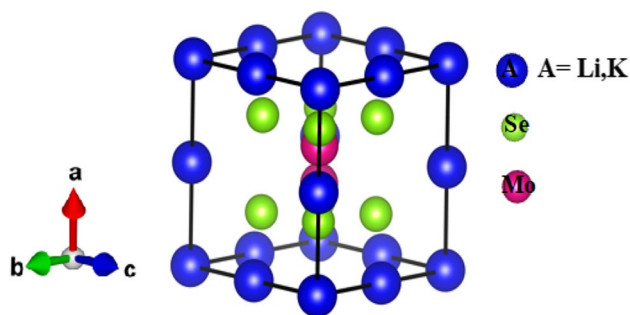
Fig. 1 Unit cell structure of A_2MoSe_4 (A=Li, K) ternary chalcogenide materials
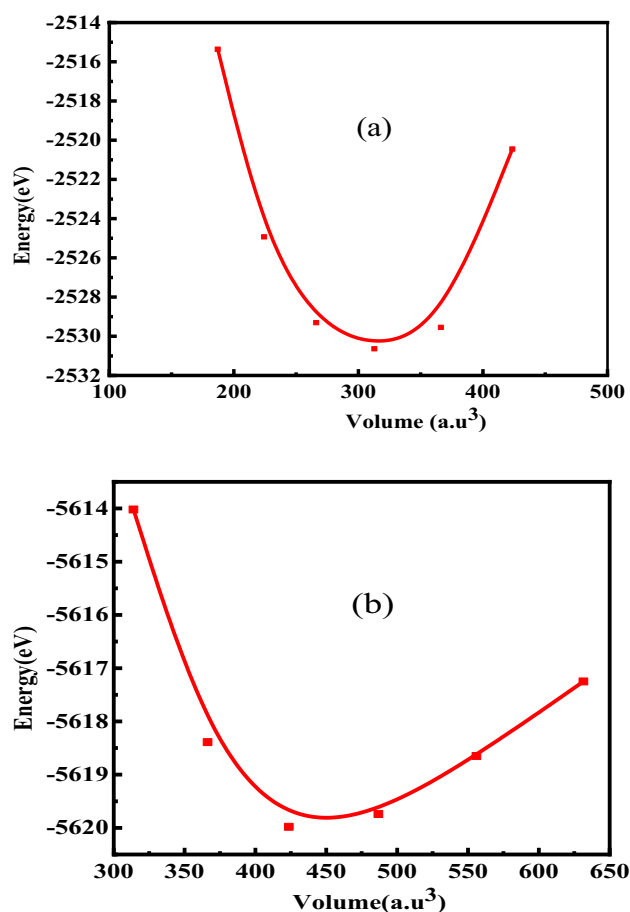
Fig. 2 The energy vs. volume optimization in the cubic phase of **a** Li_2MoSe_4 and **b** K_2MoSe_4 ternary chalcogenides

Table 1 The lattice constants a_0 (Å), ground state energy E_0 (eV), and volume at static equilibrium (V_0) and bulk modulus (B) of ternary chalcogenide compounds A_2MoSe_4 (A=Li, K)

| Material	a (Å)	V_0 (Å^3)	E_0 (eV)	B (GPa)
Li_2MoSe_4	7.62	312.85	−2530.64	19.36
K_2MoSe_4	8.43	423.61	−5619.98	63.86

at a lattice constant $a = 7.62$ (Å) for Li_2MoSe_4 and $a = 8.43$ (Å) for K_2MoSe_4 with the ground state energy (E_0) of −2530.64 eV and −5619.98 eV for Li_2MoSe_4 and K_2MoSe_4, respectively. Innovative pathways for structurally stable materials include pioneering defect engineering strategies to finely adjust chalcogenide structural stability, optimizing electronic and optical attributes, and safeguarding against structural weaknesses.

Electronic properties

Investigation of the energy band structure and the total and partial densities of states can reveal microscopic details about a variety of a material's properties and thus emphasize its ultimate potential uses. For the investigated cubic chalcogenide compounds A_2MoSe_4 (A=Li, K), the energy band dispersions along a high symmetry path in the first BZ have been calculated using the PBE-GGA, GGA+U, and HSE06 functionals. For Li_2MoSe_4 and K_2MoSe_4, with a direct band gap nature (at point G in BZ), the estimated band gaps using the PBE-GGA functional model are 0.63 and 0.71eV, respectively, as shown in Fig. 3a, b. In the instance of direct band gap hole pair recombination, an electron from the conduction band combines with a hole from the valence band. This releases energy in the form of a photon. Direct band gap semiconductors allow the transition to happen without requiring a change in momentum, which makes the recombination process less likely to be hampered by defects or other impediments in the material [45, 46]. As a result, the process happens swiftly and effectively in these materials. Direct band gap semiconductors are frequently employed in optoelectronics, such as solar cells, light-emitting diodes (LEDs), and lasers, because of their efficient direct band gap recombination mechanism [47].

PBE-GGA, GGA+U, and HSE06 all functionals were utilized to investigate the band structures of the examined compounds with better and more accurate values, as illustrated in Figs. 3, 4, and 5. The bandgap values for A_2MoSe_4 (A=Li, K) are estimated to be 2.44 eV and 2.29 eV with GGA+U and 1.32 eV and 1.66 eV with HSE06, as shown in Figs. 4 and 5. Due to the strong correlation effects among Mo-3d electrons, standard DFT calculations cannot accurately represent the electronic band gap by PBE-GGA. It is widely recognized that LDA and GGA functional underestimate the energy band gap because of the d-orbitals of Mo and self-interactions [48–50]. When used to improve the band gap and achieve a better band gap, the GGA+U approach overestimates the band gap. [51, 52]. In materials, accurate band results have always been a motivating factor. Although HSE06 hybrid functional is more expensive, it provides accurate results [53–56]. A_2MoSe_4 (A=Li, K) chalcogenide materials, distinguished by their band gap properties, stand as promising candidates for utilization in optoelectronic applications (Table 2).

**Fig. 3** The electronic band structures for **a** Li_2MoSe_4 and **b** K_2MoSe_4 using PBE-GGA
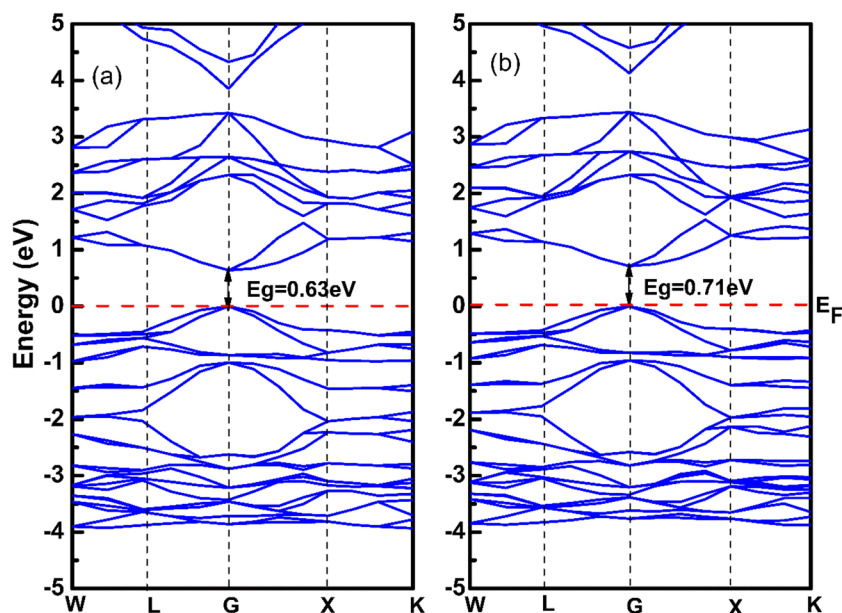
Fig. 4 The electronic band structures for **a** Li_2MoSe_4 and **b** K_2MoSe_4 using GGA+U
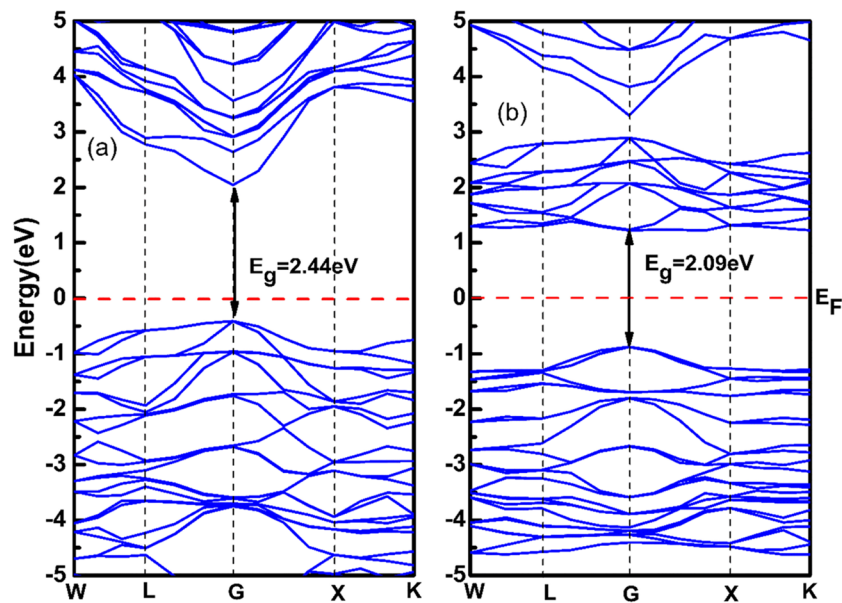
To find more information on the characteristics of interatomic chemical bonds and the nature of the orbital momentum of electronic states in the energy spectrum, we determined the partial density of states (PDOS) for A_2MoSe_4 (A=Li, K) chalcogenides while utilizing PBE-GGA functional as shown in Fig. 6a, b. Li-2s orbitals contribute mostly to the conduction states while Se-4p orbitals have participated in both the conduction and valance bands, thereby, a notable peak is found in the valance band at −2.8 eV as shown in Fig. 6a. The molybdenum 4d and 5s states contribute to DOS and show maxima at −2.9 eV in the valence band and at 1.7 eV in the conduction band close to the Fermi level. Comparatively, Mo-s orbitals have contributed less than Mo-d states. The graph shows that total PDOS rises progressively near the Fermi level in the valance band and reaches a second maximum peak at −0.8 eV mainly due to the p state of selenium atoms. The highest peak of total PDOS in the valence band is observed at −2.9 eV mainly due to Mo-p and Mo-d states. As depicted in Fig. 6b, the primary contribution of the K-2s orbitals is in the conduction region, while the Se-4p orbitals are involved in DOS across both the conduction and valence bands. Notably, the valence band displays a distinct peak at −2.8 eV. Mo-4d and Mo-5s states contribute to TDOS, exhibiting maxima at −2.6 eV and 2.5 eV in both conduction and valence bands, while the s state is less prominent than the d state. The total

Fig. 5 The electronic band structures for **a** Li$_2$MoSe$_4$ and **b** K$_2$MoSe$_4$ using HSE06
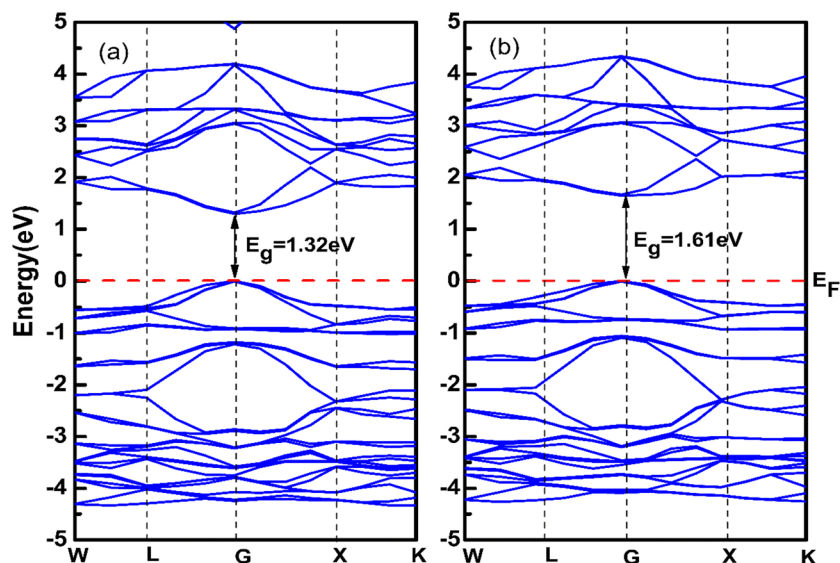
Table 2 The summary of the energy bandgap calculated through different functionals

| Materials	The energy band gap (Eg)		
	PBE-GGA	GGA+U	HSE06
Li$_2$MoSe$_4$	0.63	2.44	1.32
K$_2$MoSe$_4$	0.71	2.09	1.61

PDOS progressively rises near the Fermi level in the valence band, reaching a 2nd maximum peak at −0.23 eV, primarily attributed to the p state of selenium atoms.

Magnetic properties

As shown in Fig. 7a, b, the spin-up and spin-down channels in both regions (the valence and conduction bands) are exact replicas. It reveals a distinctive absence of net magnetic moments in both Li$_2$MoSe$_4$ and K$_2$MoSe$_4$. This phenomenon stems from the mutual cancellation of magnetic moments within each material, categorizing them as antiferromagnetic substances. The juxtaposition of magnetic forces leads to a state of equilibrium, preventing the emergence of an overall magnetic moment. The antiferromagnetic nature of both Li$_2$MoSe$_4$ and K$_2$MoSe$_4$ is clearly delineated by this graphical representation in Fig. 7a, b. The nullification of individual magnetic contributions underscores their collective antiferromagnetic character, elucidating the antiferromagnetic behavior of these materials.
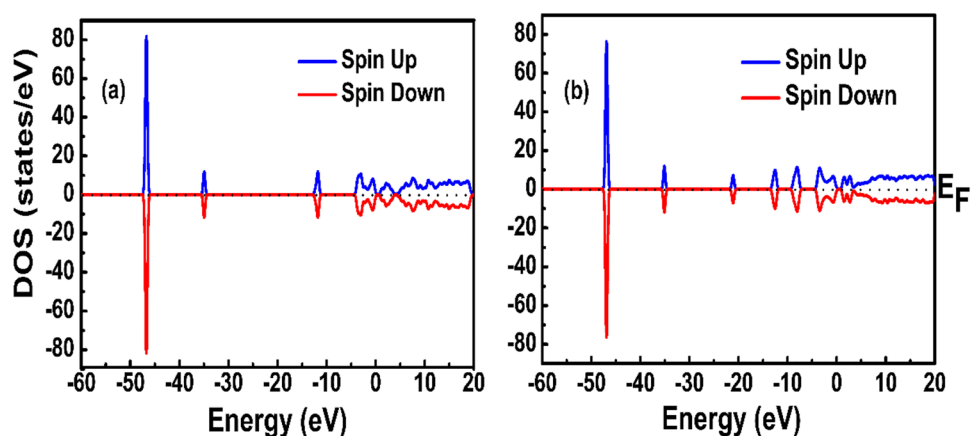
$$m = 0 \ \mu_B \tag{1}$$

As a result of their enormous potential, antiferromagnetic materials are excellent choices for the upcoming wave of
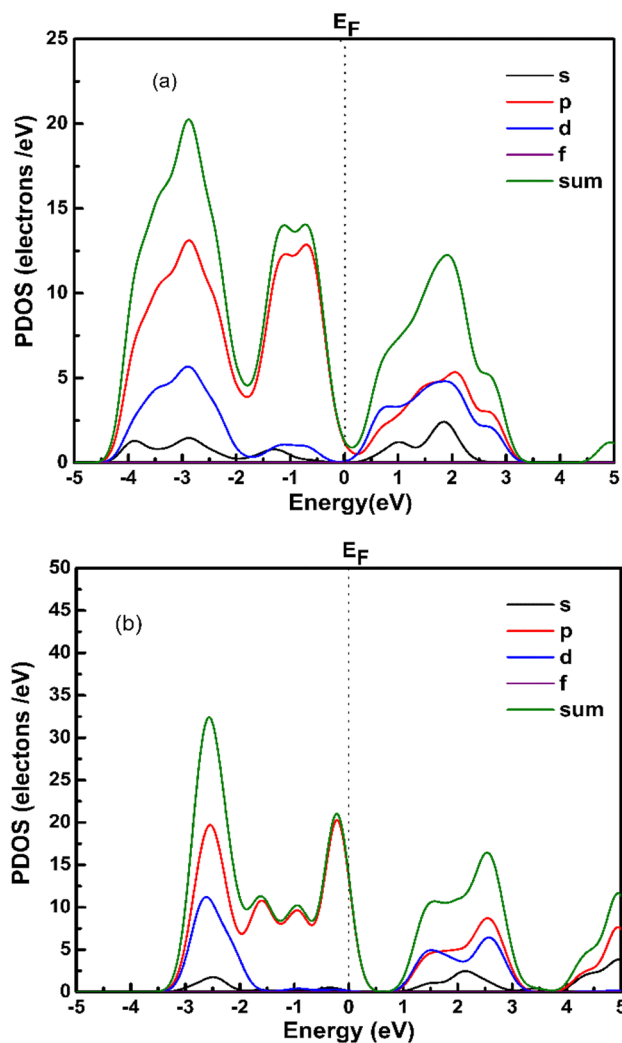
Fig. 6 PDOS for **a** Li$_2$MoSe$_4$ and **b** K$_2$MoSe$_4$ ternary chalcogenides using PBE-GGA

Fig. 7 The plots for magnetic DOS of **a** Li2MoSe4 and **b** K$_2$MoSe$_4$

spintronic applications. Antiferromagnets may supersede ferromagnets as the active spin-dependent component supporting spintronic gadgets [57].

Optical properties

Dielectric functions

The interaction of a material's surface with incident electromagnetic radiations pertains to that material's optical characteristics. The complex dielectric function elucidates the way materials respond to electromagnetic radiation. It provides information on a substance's permittivity and polarizability in relation to the density of states within the prohibited energy bad gap. Investigating the optical properties of solids such as refraction, reflection, and transmission, has proven to be a potent tool for comprehending the electronic and atomic structure of these materials [58]. The following relation can be used to describe complex dielectric functions [59].

$$\varepsilon(\omega) = \varepsilon_1(\omega) + i\varepsilon_2(\omega) \qquad (2)$$

Here, real part of the dielectric function $\varepsilon_1(\omega)$ depicts the polarization and the imaginary part of dielectric function $\varepsilon_2(\omega)$ represents the absorption. According to Fig. 8a, the static value of dielectric function $\varepsilon_1(\omega)$ are found 44.02 and 9.10 for Li$_2$MoSe$_4$ and K$_2$MoSe$_4$, respectively. Li$_2$MoSe$_4$ exhibits the highest polarization due to the static dielectric function's maximum value, pointing to an enhanced energy storage material [60, 61].

The amount of light attenuation or absorption can be calculated using the magnitude of $\varepsilon_2(\omega)$. As depicted in Fig. 8b, the imaginary part of the dielectric constant, $\varepsilon_2(\omega)$, assures how much electromagnetic radiation from incident sources is attenuated or absorbed by the material. Furthermore, the maximum absorption width is in UV region of the spectrum, which increases the significance of these materials

for optical applications. There is an apparent indication of the absorption of incident light which increases significantly and acquires ultimate sharp peaks at 2.25 eV and 2.51 eV for Li$_2$MoSe$_4$ and K$_2$MoSe$_4$, respectively. On increasing energy, it is evident that the x-axis has similar movements to $\varepsilon_2(\omega)$ between 20 and 35 eV showing only minimal absorption and fewer dispersion.

Refraction is a combination of the extinction coefficient (k) and refractive index (n), which quantifies the light's transparency and attenuation. The following equations [62] illustrate the relationship between the refractive index n (ω) and extinction coefficient k(ω) with respect to constants $\varepsilon_1(\omega)$ and $\varepsilon_2(\omega)$, respectively.

$$n^2 - k^2 = \varepsilon_1(\omega) \qquad (3)$$

$$2nk(\omega) = \varepsilon_2(\omega) \qquad (4)$$

In accordance with Fig. 8c, the refractive index n (ω) exhibits a similar trend to that of $\varepsilon_1(\omega)$, because the dielectric constant is expressed as the square of the refractive index. Moreover, it is noticed from Fig. 8d that behavior of $k(\omega)$ exhibits is comparable to that of $\varepsilon_2(\omega)$. The static values of $n(\omega)$ for Li$_2$MoSe$_4$ and K$_2$MoSe$_4$ are 3.59 and 3.01, respectively. The maximum refractive index 3.64 (for Li$_2$MoSe$_4$) and 2.95 (for K$_2$MoSe$_4$) are noticed at 0.80 eV, and 1.08 eV, respectively. Thereafter, in both cases, $n(\omega)$ steadily declines as photonic energy increases between 3 and 15 eV. In the high energy region, the group velocity exceeds the phase velocity as indicated by the fractional value of the refractive index $n(\omega)$ as illustrated in the relation [63].

$$v_g \left(1 - {}^{\lambda dn}/_{nd\lambda}\right) = v_p \qquad (5)$$

Comparatively, Li$_2$MoSe$_4$ has the highest $n(\omega)$ indicating that during light transmission, incident photons meet more valence electrons, enhancing polarization and lowering light speed.

Fig. 8 **a** dielectric real part, **b** dielectric imaginary part, **c** refractive index, and **d** extinction coefficient for A_2MoSe_4 (A=Li, K) chalcogenides
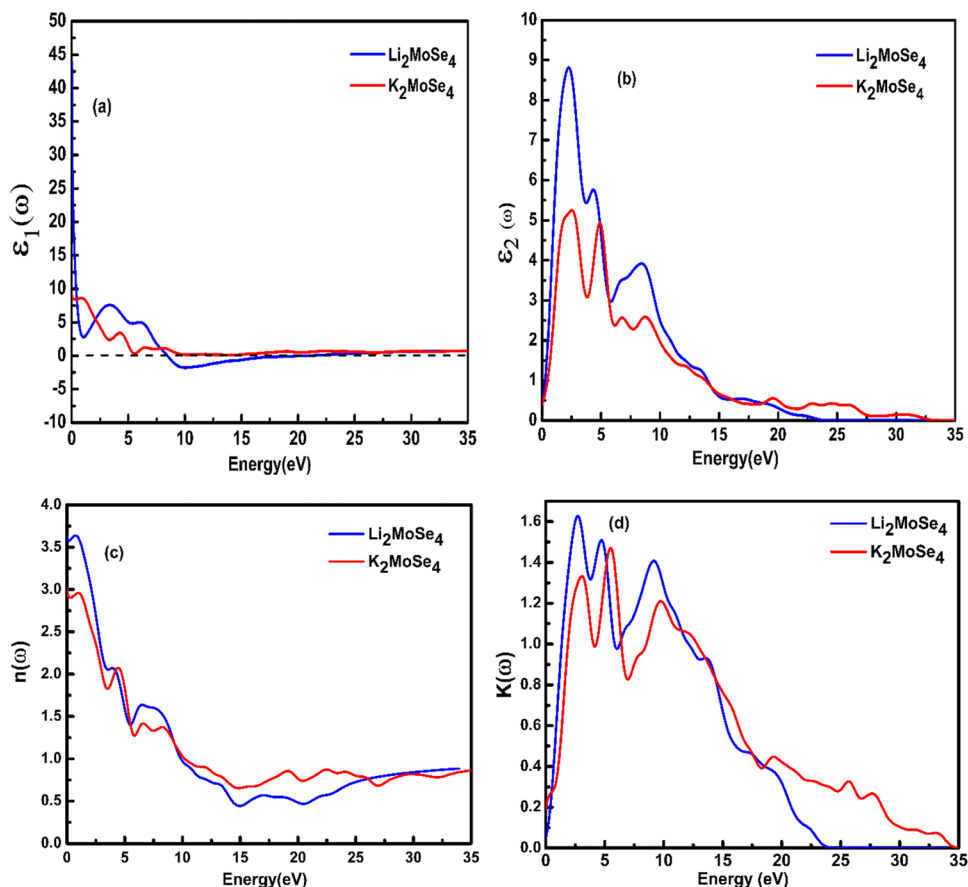
For light to be absorbed, the absorption $\alpha(\omega)$ and extinction coefficients $k(\omega)$ must be in accordance with each other by this relation [64].

$$\frac{a}{k} = \frac{4\pi}{\lambda} \qquad (6)$$

The values of the coefficient of extinction $k(\omega)$ below threshold frequency have been identified to be zero in both cases. The $k(\omega)$ initially rise, then exhibit fluctuations at energies between 2.5 and 10 eV because of transitions, and finally exhibit a declining pattern at energies between 10 and 35 eV. However, Li_2MoSe_4 has the highest extinction coefficient among the two studied compounds at 2.5 eV, making it the most absorbent material.

Absorption and loss function

A material's ability to absorb incident photons of certain energies ($E = \hbar\omega$) is dictated by its absorption coefficient $\alpha(\omega)$ [65], and its energy loss function $L(\omega)$ establishes the frequencies that correspond to the plasma resonance. When the incident radiation's frequency coincides with the plasmon frequency [66] plasma resonance occurs as shown below:

$$\alpha(\omega)_i = \frac{2\omega}{c}\left(\frac{-\text{Re}\left(\varepsilon(\omega)_i\right) + \left|\varepsilon(\omega)_i\right|}{2}\right)^{1/2} \qquad (7)$$

$$L(\omega) = \frac{\varepsilon_2(\omega)}{\varepsilon_1^2(\omega) + \varepsilon_2^2(\omega)} \qquad (8)$$

Figure 9a and b depict the computed absorption coefficients and energy loss functions. Figure 9a illustrates how all peaks have evolved from their origins and shows that there is no absorption in the absence of light or incident photon energy. Absorption increases progressively up to 9 eV. Beyond 9 eV, a fascinating and significant decrease in incident photon absorption at the material surface has been noticed in both two cases. As depicted in Fig. 9a, the significant absorption peaks for both chalcogenides that appeared close to 9 eV may be associated with plasmons. As a result, the largest values of the absorption parameters for Li_2MoSe_4 and K_2MoSe_4 have been estimated to be 19.85×10^4 cm^{-1} and 20.77×10^4 cm^{-1}, respectively, at 9 eV and 12eV energy in ultraviolet region.

The energy loss function $L(\omega)$ depicted in Fig. 9b illustrates energy loss either by scattering, dispersion, or

Fig. 9 Plots of computed **a** absorption, **b** loss function, **c** conductivity, and **d** reflectivity for A_2MoSe_4 (A=Li, K) chalcogenide
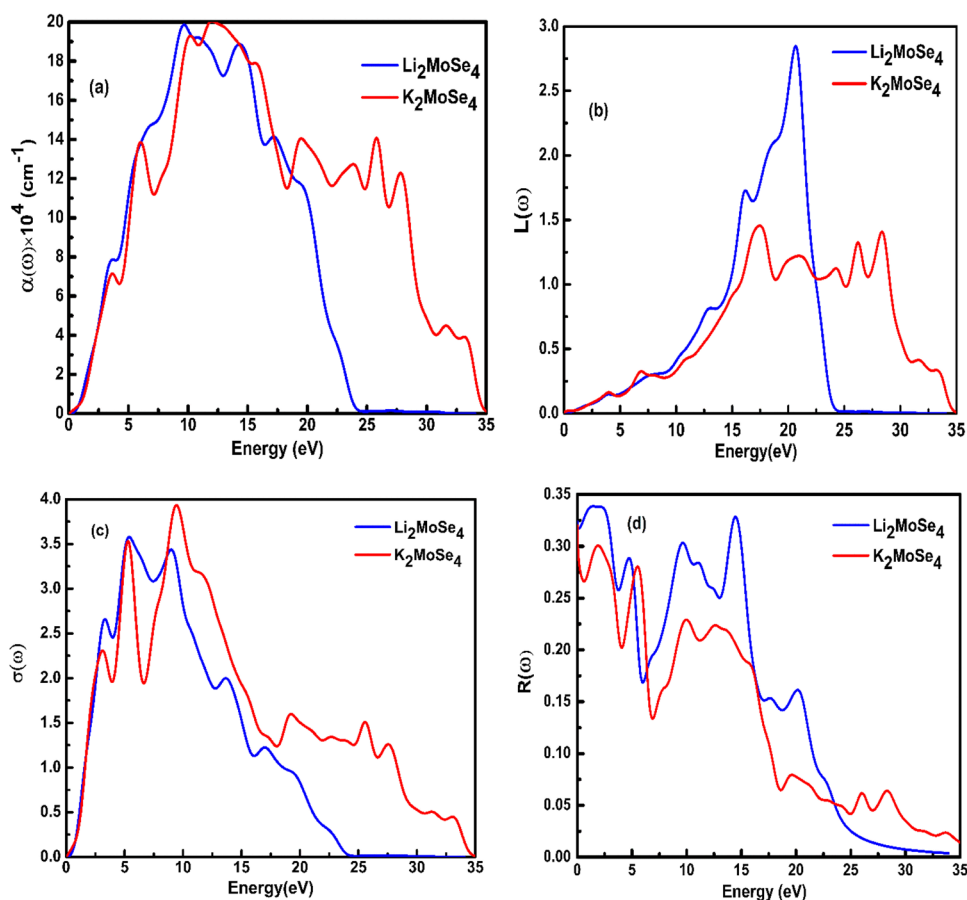
heating. It has been observed that it gradually increases up to 22 eV and then declines gradually. It is evident that the loss function first exhibits steady increase and reaches its maximum value (2.83) for Li_2MoSe_4 at about 20.76 eV. It is shown that the materials under investigation exhibit maximum absorption and minimum loss in the visible region, which renders them adequate for optoelectronic devices.

Optical conductivity and reflectivity

The optical conductivity $\sigma(\omega)$ is used to describe how well light penetrates through materials based on inter and intra-band transitions. Furthermore, it describes how bonds disintegrate when extremely energetic electromagnetic waves strike a material's surface. In Fig. 9c, optical conductivity is presented which resembles the same trend as the absorption depicted (Fig. 9a). It can be noticed that conductivity peaks when photons with a threshold frequency strike a surface. Electron-phonon (quantized lattice vibration) scattering is primarily responsible for determining the electrical conductivity of metals. As energy increases, scattering events increase, causing conductivity to decrease.

Optical conductivity rises at lower energies but diminishes at higher energies. Maximum conductivity values

for Li_2MoSe_4 and K_2MoSe_4 are 3.56 $(\Omega cm)^{-1}$ and 3.92 $(\Omega cm)^{-1}$ at 5.25 eV and 9.37eV, respectively. This behavior results from optical conductivity at low energies being dominated by electronic transitions between occupied and unoccupied states [67]. Comparative findings suggest that Li_2MoSe_4 has a distinctive conductivity, which renders it the most suited material for inclusion in optoelectronic devices.

The reflectivity of the surfaces of the compounds under consideration affects how they change behavior. Reflectivity is a measure of the energy difference between incident and reflected photons. For Li_2MoSe_4 and K_2MoSe_4, the calculated static values of reflectivity $R(\omega)$ from Fig. 9d are 0.32 and 0.33, correspondingly. The largest reflection peaks for Li_2MoSe_4 and K_2MoSe_4 are observed around 1.75 eV, where there is almost negligible absorption.

The optical results, which have been thoroughly explored, lead to the conclusion that the current chalcogenide materials are semiconducting in nature. Li_2MoSe_4 exhibits high absorption in the ultraviolent region, according to an investigation of chalcogenide's optical properties. This expands the potential of these materials for solar cells and other ultraviolent-range optical devices.

Elastic properties

The elastic parameters connect the various mechanical assets and provide strong justification for various categories of applied forces. The material is energetically and momentously illustrated by its mechanical stability, which also provides an important insight into the strength of the material for its technological uses. The mechanical parameters which are determined here include the bulk modulus, Poisson's coefficient, Pugh's ratio, anisotropy factor, Young's modulus, and shear modulus by employing Voigt–Reuss–Hill approximation. We investigate the system's mechanical stability, and the fundamental parameters for affirming the mechanical characteristics of materials. Three independent elastic constants, C_{11}, C_{12}, and C_{44} are inherent in cubic lattices as presented in Table 3 [68, 69]. Further limits on the values of the elastic constants are enforced by the requirement that the strain energy must be positive for a cubic compound [70, 71]:

$$C_{11} - C_{12} > 0, C_{44} > 0, C_{11} + 2C_{12} > 0 \qquad (9)$$

Pugh's ratios B/G determine whether a material is brittle or ductile in solids. The material is regarded as ductile if B/G > 1.75 otherwise, it is brittle [72–76]. Frantsevich et al. [77] used Poisson's ratio to differentiate brittleness and ductility, with 0.26 being the crucial value for brittle and ductile properties. The compound is brittle if the Poisson's ratio < 0.26, and ductile if the it is ≥ 0.26, as can be seen from Table 4.

Another factor that suggests a compound's brittleness and ductility is Cauchy's pressure ($C_C = C_{12}$–C_{44}) [78]. Its positive value denotes ductility, whereas a negative value depicts brittleness of any material. Thus, ductile nature of both Li_2MoSe_4 and K_2MoSe_4 chalcogenides is confirmed by the three parameters, i.e., Pugh's ratio, Poison's ratio, and Cauchy pressure.

$$G = {}^{(G_V + G_R)}\!/_2 \qquad (10)$$

In accordance to Hill approximations [79], the average shear modulus, denoted as G_H, can be calculated by averaging the Voigt (G_V) [80] and Reuss (G_R) [81] values. Table 4 shows the quantities derived from the elastic constants. We can see that both compounds have pretty much identical

Table 4 The bulk modulus B (GPa), shear modulus G (GPa), Young's modulus Y (GPa) (Voigt, Reuss and Hill), Pugh's ratio $\left(\frac{B_H}{G_H}\right)$, Poison's coefficient ($v$), Cauchy pressure ($C_C = C_{12}$-$C_{44}$), compressibility $\left(\beta = \frac{1}{B}\right)$(1/GPa), universal anisotropic index (A^U), Debye temperature (K), average sound velocity (V_m) (m/s) and anisotropic factor (A)

Parameters	Li_2MoSe_4	K_2MoSe_4
B_V	19.36120	63.86345
B_R	19.36120	63.86345
G_V	9.72804	10.53480
G_R	9.61506	4.55803
B/G	2.00	8.46
G/B	0.48	0.118
B	19.36	63.86
E	24.87	21.76
G	9.67	7.54
β	0.0516	0.0156
K	176.91	134.16
V_m	1766.65	1339.76
v	0.28	0.44
A^U	0.058	6.556
Cc (GPa)	3.14	46.31
A	0.701	0.06

Young's modulus. The following formulation is used for calculating the Young's (E), bulk (B), and shear (G) moduli:

$$E = \frac{9BG}{(3B + G)} \qquad (11)$$

$$B = \frac{B_V + B_R}{2} \qquad (12)$$

$$G = \frac{G_V + G_R}{2} \qquad (13)$$

$$G_V = \frac{3C_{44} + C_{11} - C_{12}}{5} \qquad (14)$$

$$G_R = \frac{5(C_{11} - C_{12})C_{44}}{4C_{44} + 3(C_{11} - C_{12})} \qquad (15)$$

Young's modulus determines the compound's stiffness. Its modulus data indicates a trend of Li_2MoSe_4 > K_2MoSe_4, indicating that Li_2MoSe_4 is stiffer than K_2MoSe_4. The bulk modulus data exhibits a trend K_2MoSe_4 > Li_2MoSe_4. Therefore, K_2MoSe_4 has the higher bulk modulus value indicating that it is more difficult to compress than Li_2MoSe_4. A crystal's resistance to plastic deformation is quantified by its shear modulus (modulus of

Table 3 Elastic stiffness constants C_{ij} (GPa)

Elastic constants	Li_2MoSe_4	K_2MoSe_4
C_{11}	34.082	93.01215
C_{12}	12.0008	49.28910
C_{44}	8.85300	2.98365

stiffness). The shear modulus follow the trend as Li_2MoSe_4 > K_2MoSe_4. It is apparent from the computed data that the shear modulus is lower than Young's modulus. This is because shear stress is not consistently distributed throughout the entire element cross section. The following relationship demonstrates how the two elastic constants are related.

$$E = 2G(1 + v) = 3B(1 - 2v) \qquad (16)$$

For G to be more than E, Eq. (16) requires to be less than $-1/2$. Where E is the Young's modulus of elasticity, B is the bulk modulus of elasticity, and v is the Poison's ratio. If we increase the value of the Poisson's ratio by more than half, the value of the Young's modulus will turn negative, which is not feasible. As a result, the value of the Poisson's ratio cannot be greater than half. Even though some rare materials have expected or proved negative Poisson's ratios, genuine engineering materials have positive v values [82]. As a result, in any realistic scenario, shear modulus will not be more than Young's modulus. Equation (17) defines the Poisson's ratio (v) [83].

$$v = \frac{3B - Y}{6B} \qquad (17)$$

The Poisson's ratio defines the amount of covalent or ionic bonding in a material. Table 4 demonstrates that Poisson's ratio for A_2MoSe_4 (A=Li, K) is close to 0.25 indicating that the materials have ionic nature. Most metals have v values in the range from 0.25 to 0.35 [84, 85]. For brittle covalent materials v is 0.1, whereas for ionic materials, it is 0.25. For ductile metallic materials, v is equal to 0.33. Poisson's ratio for the evaluated chalcogenide materials is almost equivalent to 0.25 (Table 4) revealing that the materials have predominately ionic character. Determining the isotropic or anisotropic nature of materials is greatly simplified by the anisotropy factor. The material is regarded as isotropic if its value is 1; otherwise, it is anisotropic [86]. Anisotropic factor relation is represented as under:

$$A = \frac{2C_{44}}{C_{11} - C_{44}} \qquad (18)$$

Another parameter "Universal Anisotropy Index" [87] also defines the isotropic or anisotropic nature of material. The universal anisotropy index is related as under:

$$A^U = 5\frac{G_V}{G_R} + \frac{B_V}{B_R} - 6 \geq 0 \qquad (19)$$

When the crystal is locally isotropic, the Eq. (19) takes a minimum value of 6. The isotropic crystal has $A^U = 0$, and its value greater and less than zero reveals crystal is anisotropic. The computed values of A^U for Li_2MoSe_4 and K_2MoSe_4 are

more than zero suggesting that both materials exhibit anisotropic behavior [88].

One of the most crucial parameters is Debye temperature (Θ_D) to determines material's thermal properties. It offers precise details regarding lattice vibration [69, 89]. Θ_D can be calculated from the following relation which can be expressed in terms of the mean sound velocity.

$$\Theta_D = \frac{h}{K}\left[\frac{3n}{4\pi}\left(\frac{N_A\rho}{M}\right)\right]^{1/3}.v_m \qquad (20)$$

where "h" denotes the Planck constant, "k" the Boltzmann constant, "N_A" the Avogadro number, "r" the density, "M" the molecular weight, "n" the number of atoms in the unit cell, and "v_m" the mean sound velocity, which could be determined using the following relation:

$$v_m = \left[\frac{1}{3}\left(\frac{2}{v_t^3} + \frac{1}{v_l^3}\right)\right]^{-1/3} \qquad (21)$$

where "v_l" and "v_t" refer to the sound velocities measured in longitudinal and transverse directions using the shear modulus G_H and the bulk modulus B, respectively:

$$v_l = \sqrt{\frac{(3B + 4G_H)}{3\rho}} \qquad (22)$$

$$v_t = \sqrt{\frac{G_H}{\rho}} \qquad (23)$$

However, we noticed a progressive decrease in mean sound velocity v_m and Θ_D values in replacing A by Li $\rightarrow$ K in A_2MoSe_4. Mattesini [90] reports a similar trend in the Sc_3EN (E=Al, Ga, In). It is noticed that our materials are elastically stable. So, they could offer several advantages in practical applications. They provide structural reliability, resist deformation under stress, and enable precise control of devices, making them indispensable in industries such as aerospace, construction, and medical devices.

Vibrational properties

It is pertinent to mention that neither experimental nor theoretical attempts have been undertaken so far to investigate the vibrational properties of these materials. As a result, it is not yet feasible to compare the computed outcomes to the literature. However, the findings of the calculated phonon frequencies might be useful for figuring out these chalcogenides dynamical and thermodynamic properties through experiment. A_2MoSe_4 (A = Li, K) comprises 14 atoms, which generate 42 phonon branches or modes of vibration;

three of these modes at zero frequency are known as acoustic modes, and the rest of 39 modes are known as optical modes of vibration.

Thirty-nine optical modes of vibration have further been identified; 12 among these modes are Raman active, 11 are IR active, and 16 computed modes have been identified to be inactive modes. Table 5 lists a representative 4 (out of 12) Raman and 4 (out of 11) IR active modes for each phase, whereas the remaining Raman and IR active modes can be referred to as degenerate modes. The maximum IR modes for Li_2MoSe_4 and K_2MoSe_4, respectively, are identified at $569 \ cm^{-1}$, and $603 \ cm^{-1}$, while the highest Raman modes are observed at 656, and $644 \ cm^{-1}$.

Figure 10a, b depicts the phonon dispersion curve and density of states for the A_2MoSe_4 (A=Li, K) materials. Only IR modes are viewed in the Li_2MoSe_4 system at low and high frequencies, while at medium frequencies, both IR and Raman modes are observed, while the contrary behavior is noted in K_2MoSe_4. Phonon DOS exhibits two distinct peaks at $90.4 \ cm^{-1}$ and $48 \ cm^{-1}$ due to Se and Li atoms motion for Li_2MoSe_4 and two prominent peaks at $109.21 \ cm^{-1}$ and $84.3 \ cm^{-1}$ for Ki_2MoSe_4 caused by Mo and Li atoms motion. At the G and X symmetry points, which are referred to as soft modes [91], the negative phonon frequencies or imaginary modes for both materials have also been observed. Unfortunately, the phonon dispersion results of Li_2MoSe_4 and K_2MoSe_4 depict the existence of imaginary phonons leading to thermal instability in specific orientation. A basic problem with lattice dynamics is indicated by the presence of imaginary frequencies in the phonon spectrum, which suggests that some vibrational modes become intrinsically unstable under thermal activation. Lattice distortions, phase changes, or even the destruction of the material's structural integrity are all possible outcomes of such thermal instability. These modes could appear as an indication of structural instability in this particular orientation [92–94]. This instability is one of the prevalent characteristics

Table 5 Phonons modes with their relative motion

Compound	Frequency	Irreducible rep	Mode	Assignment
Li_2MoSe_4	40.030997	T2g	Raman	Twisting motion
	87.247551	T2g	Raman	Rocking motion
	306.398007	T2g	Raman	Stretching due to Mo-Se atoms
	311.108475	T1u	IR	Twisting motion
K_2MoSe_4	54.046056	T1u	IR	Twisting due to Mo atoms
	84.523102	T2g	Raman	Rocking due to Mo-Se atoms
	306.346235	T2g	Raman	Stretching due to Mo-Se atoms
	377.135304	T1u	IR	Twisting
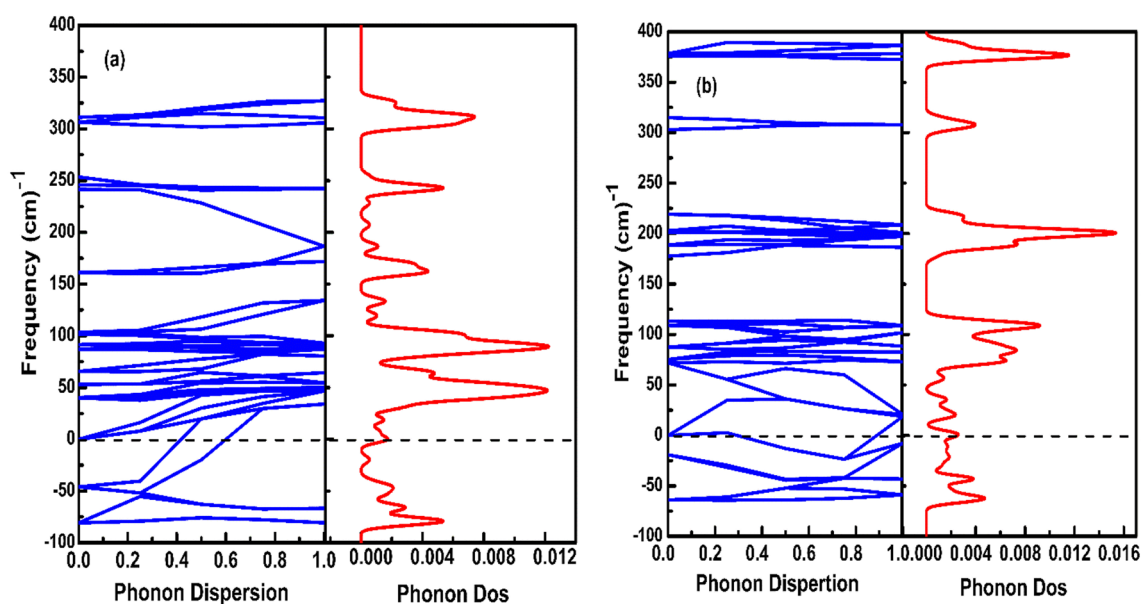
Fig. 10 Plots of calculated Phonon dispersion **a** Li_2MoSe_4 and **b** K_2MoSe_4

Fig. 11 Modes of Vibrations for frequency **a** 40 cm^{-1}, **b** 87 cm^{-1}, **c** 306cm $^{-1}$, **d** 311 cm^{-1} for Li$_2$MoSe$_4$


(a)

(b)

(c)

(d)
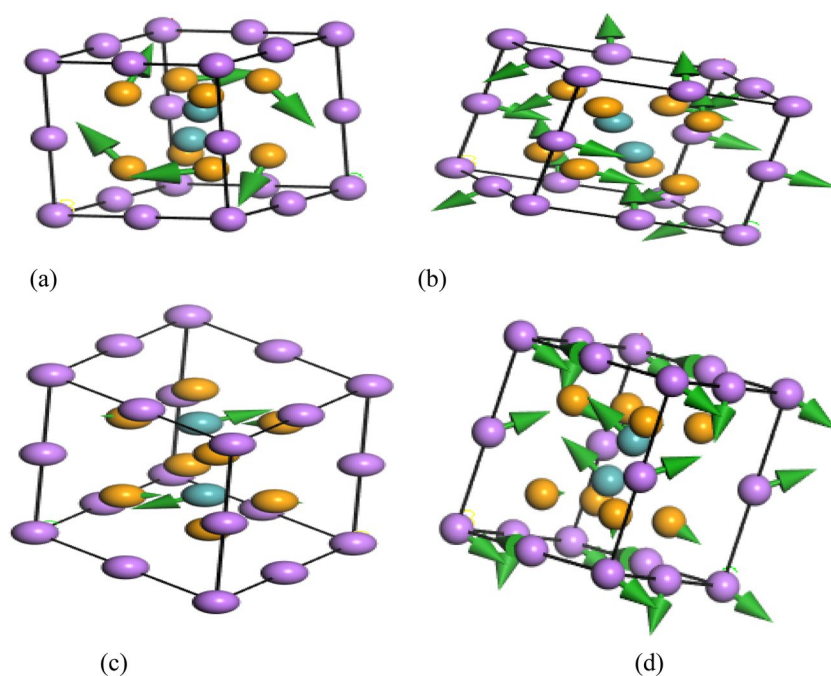
found in these chalcogenide structures which reflect the antiferroelectric distortion due to the tilting or rotation of octahedra in the neighboring primitive cells [95, 96]. Modes of vibrations for different frequencies shown in Fig. 11 and 12 are summarized in Table 5.

Thermodynamics properties

The harmonic approximation method through CASTEP code is utilized to figure out the thermodynamic attributes of the chalcogenide's materials under investigation. By computing thermodynamic characteristics, it is conceivable to validate

Fig. 12 Modes of vibrations for frequency **a** 54 cm^{-1}, **b** 84 cm^{-1}, **c** 306 cm^{-1}, and d 377 cm^{-1} for K$_2$MoSe$_4$ chalcogenide

(a)

(b)

(c)

(d)
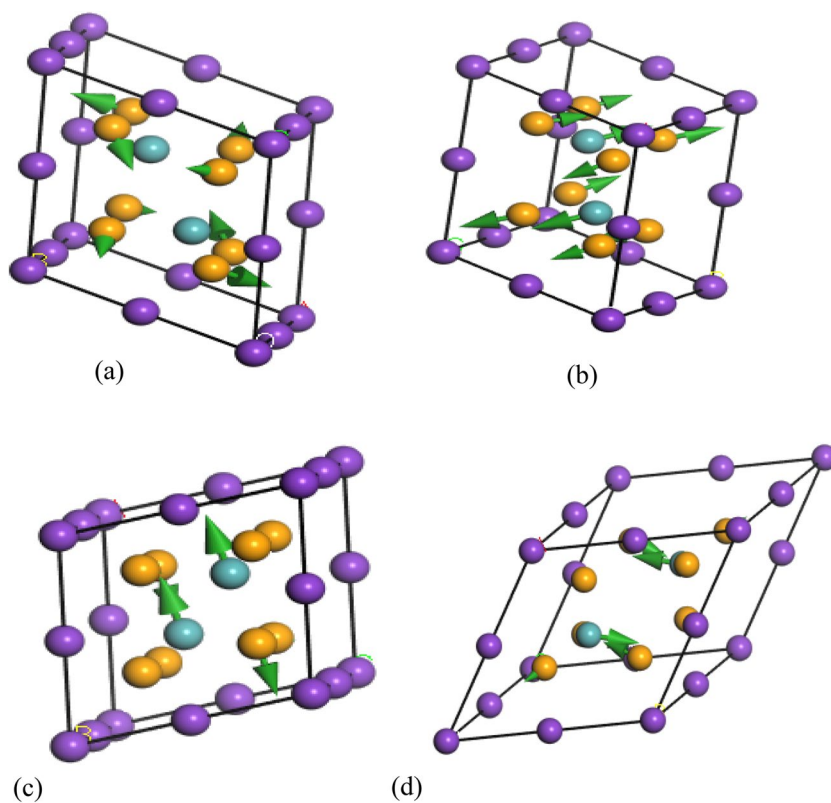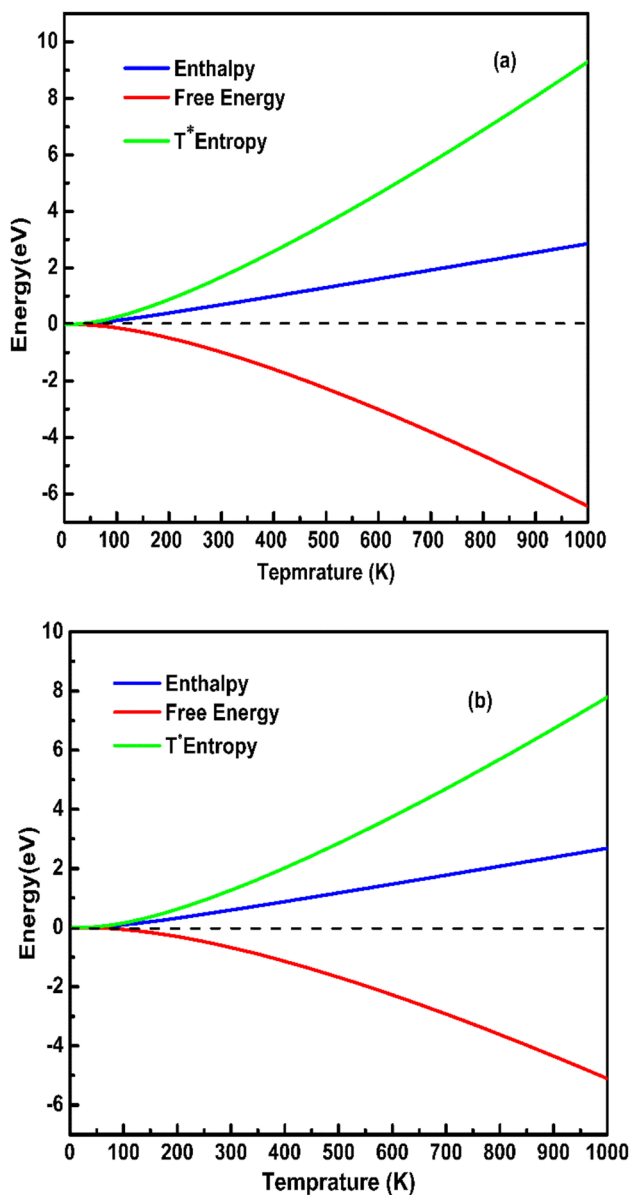
Fig. 13 The calculated thermodynamic parameters for **a** Li_2MoSe_4 and **b** K_2MoSe_4 chalcogenides

Fig. 14 Calculated heat capacity of A_2MoSe_4 (A=Li, K) chalcogenides

Li_2MoSe_4. It is therefore noteworthy to draw attention to the fact that comparatively Li_2MoSe_4 appears more stable as the temperature increases. Li_2MoSe_4 and K_2MoSe_4 have maximal free energy values of −6.44 eV and −5.11 eV, respectively, at 1000 K. The highest values for the thermodynamic parameter, temperature times entropy, have been obtained as 7.79 eV and 9.29 eV at 1000 K for Li_2MoSe_4 and K_2MoSe_4, respectively.

It is apparent that the heat capacity (C_v) increases as the temperature increases. It attains its classical limit at 600 K as depicted in Fig. 14. C_v for K_2MoSe_4 is lower than that of the Li_2MoSe4 at any temperature. Material with higher C_v signifies that a substance can absorb and store more heat energy, making it more effective at regulating temperature and storing thermal energy. It is evident from the Figs. 13 and 14 that Li_2MoSe_4 is thermodynamically more stable than K_2MoSe_4 making it a better choice for an extensive variety of applications.

Conclusions

This research has been carried out to gain a thorough understanding of the structural, optoelectronic, magnetic, elastic, vibrational, and thermodynamic properties of cubic Li_2MoSe_4 and K_2MoSe_4 structures using the CASTEP code. These are found to have stable structures with ground state energies of −2530.64 eV at volume 312.85 ($Å^3$) and −5619.98 eV at volume 423.61 ($Å^3$), respectively. These have direct band gap of 1.32 eV and 1.61 eV, respectively when HSE06 functional is used which classifies them as semiconductors. To validate band gap accuracy, GGA+U and PBE-GGA are also used; however, it is concluded that HSE06 functional gives more

the thermal stability of these cubic phase chalcogenides [97, 98]. The graphs in Fig. 13a and b demonstrate the thermodynamic properties of Li_2MoSe_4 and K_2MoSe_4 with temperature range of 0 to 1000 K. Linear behavior is observed for the enthalpy. The relationship between the Helmholtz free energy (F), internal energy (U), and entropy (S) is expressed by the following thermodynamic equation [99].

$$TS = U - F \qquad (24)$$

For Li_2MoSe_4 and K_2MoSe_4, the maximum enthalpy values are 2.85 eV and 2.68 eV at 1000 K, respectively. In contrast to K_2MoSe_4, free energy diminishes faster with

precise and accurate results. We feel driven to declare that these are excellent candidates for optoelectronic applications due to their ability to efficiently absorb ultraviolet radiation. The mechanical characteristics of both chalcogenide materials demonstrate that their elastic parameters support their ductile behavior and witness their heightened stability. Their phonon dispersion results unveiled an imaginary phonon indicating thermal instability. This investigation strengthens the belief that these materials are effective for producing photovoltaics, and spintronics. Our findings set the stage for further investigations into the physical properties of ternary transition metal chalcogenides.

Data availability The data that support the findings of this study are available on request from the corresponding author. The data are not publicly available due to privacy or ethical restrictions.

Declarations

Ethical approval This declaration is "not applicable".

References

1. Lu JM, Zheliuk O, Leermakers I, Yuan NF, Zeitler U, Law KT, Ye J (2015) Evidence for two-dimensional Ising superconductivity in gated MoS_2. Science 350(6266):1353–1357
2. Lai X, Zhang H, Wang Y, Wang X, Zhang X, Lin J, Huang F (2015) Observation of superconductivity in tetragonal FeS. J Am Chem Soc 137(32):10148–10151
3. Imai H, Shimakawa Y, Kubo Y (2001) Large thermoelectric power factor in TiS_2 crystal with nearly stoichiometric composition. Phys Rev B 64(24):241104
4. Wu J, Schmidt H, Amara KK, Xu X, Eda G, Ozyilmaz B (2014) Large thermoelectricity via variable range hopping in chemical vapor deposition grown single-layer MoS_2. Nano Lett 14(5):2730–2734
5. Sugai S (1985) Lattice vibrations in the charge-density-wave states of layered transition metal dichalcogenides. Phys. Status Solidi B Basic Res 129(1):13–39
6. Solorza-Feria O, Ellmer K, Giersig M, Alonso-Vante N (1994) Novel low-temperature synthesis of semiconducting transition metal chalcogenide electrocatalyst for multielectron charge transfer: molecular oxygen reduction. Electrochim Acta 39(11-12):1647–1653
7. Chia X, Sofer Z, Luxa J, Pumera M (2017) Layered noble metal dichalcogenides: tailoring electrochemical and catalytic properties. ACS Appl Mater Interfaces 9(30):25587–25599
8. Sakamoto T, Wakeshima M, Hinatsu Y, Matsuhira K (2007) Charge-density-wave superconductor $Bi_2Rh_3Se_2$. Phys Rev B 75(6):060503
9. Robbins M, Willens RH, Miller RC (1967) Superconductivity in the spinels $CuRh_2S_4$ and $CuRh_2Se_4$. Solid State Commun 5(12):933–934
10. Trump BA, Tutmaher JA, McQueen TM (2015) Anion–anion bonding and topology in ternary iridium seleno–stannides. Inorg Chem 54(24):11993–12001
11. Guo Z, Sun F, Yuan W (2017) Chemical intercalations in layered transition metal chalcogenides: syntheses, structures, and related properties. Cryst Growth Des 17(4):2238–2253
12. Rouxel J (1979) Alkali metal intercalation compounds of transition metal chalcogenides: TX_2, TX_3 and TX_4 chalcogenides. Intercalated Layered Materials. Springer Netherlands, Dordrecht, pp 201–250
13. Murphy DW, Sunshine SA, Zahurak SM (1987) Preparation methods for alkali metal intercalation compounds of oxides and chalcogenides. Chemical Physics of Intercalation. Springer US, Boston, MA, pp 173–179
14. Sturza M, Malliakas CD, Bugaris DE, Han F, Chung DY, Kanatzidis MG (2014) $NaCu_6Se_4$: a layered compound with mixed valency and metallic properties. Inorg Chem 53(22):12191–12198
15. Sturza M, Bugaris DE, Malliakas CD, Han F, Chung DY, Kanatzidis MG (2016) Mixed-valent $NaCu_4Se_3$: a two-dimensional metal. Inorg Chem 55(10):4884–4890
16. Chen H, Rodrigues JN, Rettie AJ, Song TB, Chica DG, Su X et al (2018) High hole mobility and nonsaturating giant magnetoresistance in the new 2d metal nacu4se4 synthesized by a unique pathway. J Am Chem Soc 141(1):635–642
17. Ma N, Li YY, Chen L, Wu LM (2020) α-$CsCu_5Se_3$: discovery of a low-cost bulk selenide with high thermoelectric performance. J Am Chem Soc 142(11):5293–5303
18. Stoliaroff A, Jobic S, Latouche C (2020) An ab initio perspective on the key defects of cscu5se3, a possible material for optoelectronic applications. J Phys Chem C 124(8):4363–4368
19. Buffiere M, Dhawale DS, El-Mellouhi F (2019) Chalcogenide materials and derivatives for photovoltaic applications. Energy Technology 7(11):1900819
20. Kuhar K, Crovetto A, Pandey M, Thygesen KS, Seger B, Vesborg PC et al (2017) Sulfide perovskites for solar energy conversion applications: computational screening and synthesis of the selected compound $LaYS_3$. Energy Environ Sci 10(12):2579–2593
21. Perera S, Hui H, Zhao C, Xue H, Sun F, Deng C et al (2016) Chalcogenide perovskites–an emerging class of ionic semiconductors. Nano Energy 22:129–135
22. Niu, S., Huyan, H., Liu, Y., Yeung, M., Ye, K., Blankemeier, L., ... & Ravichandran, J. (2018). Band-gap control via structural and chemical tuning of transition metal perovskite chalcogenides. arXiv preprint arXiv:1804.09362.
23. Sun Q, Chen H, Yin WJ (2018) Do chalcogenide double perovskites work as solar cell absorbers: a first-principles study. Chem Mater 31(1):244–250
24. Swarnkar A, Mir WJ, Chakraborty R, Jagadeeswararao M, Sheikh T, Nag A (2019) Are chalcogenide perovskites an emerging class of semiconductors for optoelectronic properties and solar cell? Chem Mater 31(3):565–575
25. Palos E, Reyes-Serrato A, Alonso-Nuñez G, Sánchez JG (2020) Modeling the ternary chalcogenide Na_2MoSe_4 from first-principles. J Phys Condens Matter 33(2):025501
26. Jain A, Ong SP, Hautier G, Chen W, Richards WD, Dacek S et al (2013) Commentary: The materials project: a materials genome approach to accelerating materials innovation. APL Mater 1(1)
27. Mebarki SH, Amrani B, Khodja KD, Khelil A (2017) The optoelectronic properties of a solar energy material: Ag_2HgSnS_4. IOP Conference Series: Materials Science and Engineering (Vol. 186, No. 1). IOP Publishing, p 012026
28. Clark SJ, Segall MD, Pickard CJ, Hasnip PJ, Probert MI, Refson K, Payne MC (2005) First principles methods using CASTEP. Zeitschrift für kristallographie-crystalline materials 220(5-6):567–570
29. Kohn W, Sham LJ (1965) Self-consistent equations including exchange and correlation effects. Phys Rev 140(4A):A1133
30. Hamann DR, Schlüter M, Chiang C (1979) Norm-conserving pseudopotentials. Phys Rev Lett 43(20):1494
31. Hamann DR (1989) Generalized norm-conserving pseudopotentials. Phys Rev B 40(5):2980

32. Troullier N, Martins JL (1991) Efficient pseudopotentials for plane-wave calculations. Phys Rev B *43*(3):1993

33. Perdew JP, Burke K, Ernzerhof M (1996) Generalized gradient approximation made simple. Phys Rev Lett 77(18):3865

34. Fatheema J, Fatima M, Monir NB, Khan SA, Rizwan S (2020) A comprehensive computational and experimental analysis of stable ferromagnetism in layered 2D Nb-doped Ti_3C_2 MXene. Phys E: Low-Dimens Syst Nanostructures 124:114253

35. Heyd J, Scuseria GE, Ernzerhof M (2003) Hybrid functionals based on a screened Coulomb potential. J Chem Phys 118(18):8207–8215

36. Monkhorst HJ, Pack JD (1976) Special points for Brillouin-zone integrations. Phys Rev B 13(12):5188

37. Hohenberg P, Kohn W (1964) Inhomogeneous electron gas. Phys Rev 136(3B):B864

38. Rong Z, Zhi C, Jun C (2022) Ab initio calculation of mechanical, electronic and optical characteristics of chalcogenide perovskite BaZrS3 at high pressures. Acta Crystallogr C Struct Chem 78(10)

39. Xiong K, Robertson J, Clark SJ (2006) Defect states in the high-dielectric-constant gate oxide $LaAlO_3$. Appl Phys Lett 89(2)

40. Ismaıl WB, Mainprice D (1998) An olivine fabric database: an overview of upper mantle fabrics and seismic anisotropy. Tectonophysics 296(1-2):145–157

41. Hadi MA, Roknuzzaman M, Chroneos A, Naqib SH, Islam AKMA, Vovk RV, Ostrikov K (2017) Elastic and thermodynamic properties of new (Zr3− xTix) AlC_2 MAX-phase solid solutions. Comput Mater Sci 137:318–326

42. Gonze X, Lee C (1997) Dynamical matrices, Born effective charges, dielectric permittivity tensors, and interatomic force constants from density-functional perturbation theory. Phys Rev B 55(16):10355

43. Kral J, Lukes J, Netuka I, Vesely J (eds) (2011) Potential theory-ICPT 94: proceedings of the international conference on potential theory held in Kouty, Czech Republic, August 13-20, 1994. Walter de Gruyter

44. Murnaghan FD (1944) The compressibility of media under extreme pressures. Proc Natl Acad Sci 30(9):244–247

45. Kumar A, Ahluwalia PK (2012) Electronic structure of transition metal dichalcogenides monolayers 1H-MX_2 (M= Mo, W; X= S, Se, Te) from ab-initio theory: new direct band gap semiconductors. Eur Phys J B 85:1–7

46. Bala A, Kumar V (2021) Direct band gap halide-double-perovskite absorbers for solar cells and light emitting diodes: ab initio study of bulk and layers. Phys Rev Mater 5(9):095401

47. Lee IH, Oh YJ, Kim S, Lee J, Chang KJ (2016) Ab initio materials design using conformational space annealing and its application to searching for direct band gap silicon crystals. Comput Phys Commun 203:110–121

48. Germaneau É, Su G, Zheng QR (2013) Implementation of the modified Becke–Johnson meta-GGA functional in Quantum Espresso. Comput Phys Commun 184(7):1697–1700

49. Morales-García Á, Valero R, Illas F (2017) An empirical, yet practical way to predict the band gap in solids by using density functional band structure calculations. J Phys Chem C 121(34):18862–18866

50. Tran, F., Blaha, P., & Schwarz, K. (2007). Band gap calculations with Becke–Johnson exchange potential. J Phys Condens Matter, 19(19), 196208.

51. Shao G (2009) Red shift in manganese-and iron-doped TiO_2: a DFT+ U analysis. J Phys Chem C 113(16):6800–6808

52. Tompsett DA, Middlemiss DS, Islam MS (2012) Importance of anisotropic Coulomb interactions and exchange to the band gap and antiferromagnetism of β-MnO_2 from DFT+ U. Phys Rev B 86(20):205126

53. Vines F, Lamiel-García O, Chul Ko K, Yong Lee J, Illas F (2017) Systematic study of the effect of HSE functional internal parameters on the electronic structure and band gap of a representative set of metal oxides. J Comput Chem 38(11):781–789

54. Na GS, Jang S, Lee YL, Chang H (2020) Tuplewise material representation based machine learning for accurate band gap prediction. J Phys Chem A 124(50):10616–10623

55. Bashyal K, Pyles CK, Afroosheh S, Lamichhane A, Zayak AT (2018) Empirical optimization of DFT+ U and HSE for the band structure of ZnO. J Phys Condens Matter 30(6):065501

56. Xiao H, Tahir-Kheli J, Goddard III WA (2011) Accurate band gaps for semiconductors from density functional theory. The Journal of Physical Chemistry Letters 2(3):212–217

57. Jungwirth T, Marti X, Wadley P, Wunderlich J (2016) Antiferromagnetic spintronics. Nat Nanotechnol 11(3):231–241

58. Caid M, Rached D, Al-Qaisi S, Rached Y, Rached H (2023) DFT calculations on physical properties of the lead-free halide-based double perovskite compound $Cs_2CdZnCl_6$. Solid State Commun 369:115216

59. Bouarissa A, Gueddim A, Bouarissa N, Maghraoui-Meherzi H (2020) Optical spectra of monolayer MoS2 from spin-polarized all electrons density-functional calculations. Optik 222:165477

60. Caid M, Rached H, Bentouaf A, Rached D, Rached Y (2021) High-throughput study of the structural, electronic, and optical properties of short-period (BeSe) m/(ZnSe) n superlattices based on DFT calculations. Computational Condensed Matter 29:e00598

61. Caid M, Rached D, Cheref O, Righi H, Rached H, Benalia S et al (2019) Full potential study of the structural, electronic and optical properties of (InAs) m/(GaSb) n superlattices. Computational Condensed Matter 21:e00394

62. Sabir B, Murtaza G, Khalil RA, Mahmood Q (2019) First principle study of electronic, mechanical, optical and thermoelectric properties of $CsMO_3$ (M= Ta, Nb) compounds for optoelectronic devices. J Mol Graph Model 86:19–26

63. Mahmood Q, Rashid M, Noor NA, Ashiq MGB, Ramay SM, Mahmood A (2019) Opto-electronic and thermoelectric properties of $MgIn_2X_4$ (X= S, Se) spinels via ab-initio calculations. J Mol Graph Model 88:168–173

64. Wooten F (1972) Optical properties of solids. Academic Press

65. Hilal M, Rashid B, Khan SH, Khan A (2016) Investigation of electro-optical properties of InSb under the influence of spin-orbit interaction at room temperature. Mater Chem Phys 184:41–48

66. Bouarissa A, Gueddim A, Bouarissa N, Maghraoui-Meherzi H (2020) Optical response and magnetic moment of MoS_2 material. Optik 208:164080

67. Caid M, Rached D (2020) First-principles calculations to investigate structural, electronic and optical properties of (AlSb) m/(GaSb) n superlattices. Mater Sci-Pol 38(2):320–327

68. Mattesini M, Ahuja R, Johansson B (2003) Cubic Hf_3N_4 and Zr_3N_4: a class of hard materials. Phys Rev B 68(18):184108

69. Mattesini M, Soler JM, Yndurain F (2006) Ab initio study of metal-organic framework-5 Zn_4O (1, 4− benzenedicarboxylate) 3: an assessment of mechanical and spectroscopic properties. Phys Rev B *73*(9):094111

70. Eriksson, O. (2004). Electronic structure calculations of phase stability: cohesive and elastic properties.

71. Gueddim A, Bouarissa N, Gacem L, Villesuzanne A (2018) Structural phase stability, elastic parameters and thermal properties of YN from first-principles calculation. Chin J Phys 56(5):1816–1825

72. Nazir S, Mahmood I, Noor NA, Laref A, Sajjad M (2019) Ab-initio simulations of MgTiO3 oxide at different pressure. High Energy Density Phys 33:100715

73. Qureshi MW, Ma X, Tang G, Paudel R (2020) Structural stability, electronic, mechanical, phonon, and thermodynamic properties of the M_2GaC (M= Zr, Hf) max phase: an AB initio calculation. Materials 13(22):5148

74. Mo Y, Rulis P, Ching WY (2012) Electronic structure and optical conductivities of 20 MAX-phase compounds. Phys Rev B 86(16):165122

75. Hussain MI, Khalil RA, Hussain F, Imran M, Rana AM, Kim S (2020) Investigations of structural, electronic and optical properties of $YInO_3$ (Y= Rb, Cs, Fr) perovskite oxides using mBJ approximation for optoelectronic applications: a first principles study. Mater Sci Semicond Process 113:105064

76. Ali MA, Hossain MM, Islam AKMA, Naqib SH (2021) Ternary boride Hf_3PB_4: Insights into the physical properties of the hardest possible boride MAX phase. J Alloys Compd 857:158264

77. Murtaza G, Sajid A, Rizwan M, Takagiwa Y, Khachai H, Jibran M et al (2015) First principles study of Mg_2X (X= Si, Ge, Sn, Pb): elastic, optoelectronic and thermoelectric properties. Mater Sci Semicond Process 40:429–435

78. Sofi SA, Yousuf S, Bhat TM, Nabi M, Singh S, Saleem Z et al (2019) Investigation of structural and mechanical properties of ferromagnetic Co_2MnAs compound. AIP Conference Proceedings (Vol. 2115, No. 1). AIP Publishing

79. Wu SQ, Hou ZF, Zhu ZZ (2007) Ab initio study on the structural and elastic properties of MAlSi (M= Ca, Sr, and Ba). Solid State Commun 143(8-9):425–428

80. Hu WC, Liu Y, Li DJ, Zeng XQ, Xu CS (2013) Mechanical and thermodynamic properties of Al3Sc and Al3Li precipitates in Al–Li–Sc alloys from first-principles calculations. Phys B Condens Matter 427:85–90

81. Guo Y, Wang W, Huang H, Zhao H, Jing Y, Yi G et al (2020) Effect of doping Zn atom on the structural stability, mechanical and thermodynamic properties of AlLi phase in Mg–Li alloys from first-principles calculations. Philos Mag 100(14):1849–1867

82. The physics and chemistry of materials: 9780471057949, Joel I. Gersten, Frederick W. Smith ISBN: 978-0-471-05794-9

83. Shein IR, Ivanovskii AL (2008) Elastic properties of mono-and polycrystalline hexagonal AlB2-like diborides of s, p and d metals from first-principles calculations. J Phys Condens Matter 20(41):415218

84. Wu ZJ, Zhao EJ, Xiang HP, Hao XF, Liu XJ, Meng J (2007) Crystal structures and elastic properties of superhard IrN_2 and IrN_3 from first principles. Phys Rev B 76(5):054115

85. Haines J, Leger JM, Bocquillon G (2001) Synthesis and design of superhard materials. Annu Rev Mater Res 31(1):1–23

86. Candan A, Akbudak S, Uğur Ş, Uğur G (2019) Theoretical research on structural, electronic, mechanical, lattice dynamical and thermodynamic properties of layered ternary nitrides Ti_2AN (A= Si, Ge and Sn). J Alloys Compd 771:664–673

87. Naher MI, Naqib SH (2021) An ab-initio study on structural, elastic, electronic, bonding, thermal, and optical properties of topological Weyl semimetal TaX (X= P, As). Sci Rep 11(1):5592

88. Ledbetter H, Migliori A (2006) A general elastic-anisotropy measure. J Appl Phys 100(6)

89. Slack GA, Tanzilli RA, Pohl RO, Vandersande JW (1987) The intrinsic thermal conductivity of AlN. J Phys Chem Solids 48(7):641–647

90. Mattesini M, Magnuson M, Tasnadi F, Höglund C, Abrikosov IA, Hultman L (2009) Elastic properties and electrostructural correlations in ternary scandium-based cubic inverse perovskites: a first-principles study. Phys Rev B 79(12):125122

91. Brivio F, Frost JM, Skelton JM, Jackson AJ, Weber OJ, Weller MT et al (2015) Lattice dynamics and vibrational spectra of the orthorhombic, tetragonal, and cubic phases of methylammonium lead iodide. Phys Rev B 92(14):144308

92. Benedek NA, Fennie CJ (2013) Why are there so few perovskite ferroelectrics? J Phys Chem C 117(26):13339–13349

93. Friák M, Holec D, Šob M (2018) An ab initio study of mechanical and dynamical stability of $MoSi_2$. J Alloys Compd 746:720–728

94. Li Z, Zhang Y, Peng C (2009) Ab initio study on the ground states, phase stability, and mechanical properties of the Au–Pt system. Solid State Commun 149(23-24):952–956

95. Da Silva EL, Skelton JM, Parker SC, Walsh A (2015) Phase stability and transformations in the halide perovskite $CsSnI_3$. Phys Rev B 91(14):144107

96. Hussain MI, Khalil RA, Boota S, Hussain F, Imran M, Murtaza G et al (2020) The structural, electronic and dynamical investigations of $NdMn_2O_5$ and La_2CoMnO_6 for optoelectronic applications: a first principles study. Optik 204:164165

97. Khalil RMA, Hussain F, Rana AM, Imran M, Murtaza G (2019) Comparative study of polytype 2H-MoS_2 and 3R-MoS_2 systems by employing DFT. Physica E: low-dimensional Systems and Nanostructures 106:338–345

98. Coutinho SS, Tavares MS, Barboza CA, Frazão NF, Moreira E, Azevedo DL (2017) 3R and 2H polytypes of MoS_2: DFT and DFPT calculations of structural, optoelectronic, vibrational and thermodynamic properties. J Phys Chem Solids 111:25–33

99. Atkins PW, de Paula J, Keeler MA (2018) Physical chemistry 11th edn. Oxford University Press